Minor embedding with Stuart-Landau oscillator networks

S. L. Harrison,[1, *] H. Sigurdsson,[2, 1] and P. G. Lagoudakis[3, 1]

[1]*School of Physics and Astronomy, University of Southampton, Southampton, SO17 1BJ, United Kingdom*
[2]*Science Institute, University of Iceland, Dunhagi 3, IS-107, Reykjavik, Iceland*
[3]*Hybrid Photonics Laboratory, Skolkovo Institute of Science and Technology,*
Territory of Innovation Center Skolkovo, 6 Bolshoy Boulevard 30, Bld. 1, 121205 Moscow, Russia
(Dated: October 12, 2022)

We theoretically implement a strategy from quantum computation architectures to simulate Stuart-Landau oscillator dynamics in all-to-all connected networks, also referred to as complete graphs. The technique builds upon the triad structure minor embedding which expands dense graphs of interconnected elements into sparse ones which can potentially be realized in future on-chip solid state technologies with tunable edge weights. As a case study, we reveal that the minor embedding procedure allows simulating the XY model on complete graphs, thus bypassing a severe geometric constraint.

I. INTRODUCTION

Solving dense graph combinatorial optimization problems has been studied thoroughly in the field of quantum annealing, where qubits and their relative coupling strengths represent graph vertices and edge weights respectively. To solve arbitrary graph problems using pre-existing qubit architectures, dense graphs can be embedded into new representative graphs using gauge field constraints [1, 2], or connected ferromagnetic subgraphs using *minor embedding* techniques [3–8]. In the latter, a standardized minor embedding to the *triad structure* is commonly used, allowing any all-to-all connected (dense) graph to be mapped to a planar qubit architecture [3, 9, 10].

In this study, we investigate the feasibility of using minor embedding to a triad structure [3, 10] to simulate the dynamics in dense networks of interacting classical oscillators instead of qubits. Our study is motivated by the recent developments in designing analogue computing strategies based on optical oscillatory networks to heuristically solve complex graph problems across various platforms such as: Exciton-polariton condensates [11–16], photon condensates [17], non-degenerate optical parametric oscillators [18–20], photon down-conversion oscillators [21], and coupled microlaser arrays [22, 23]. Even digital computer algorithms designed to efficiently solve the dynamics of oscillatory networks have displayed impressive prowess in combinatorial optimization [24, 25].

Optical platforms for unconventional analogue computation [21] have many desirable properties such as photonic parallelism, low cross-talk, ultrafast timescales (i.e., high sampling rate), and low power consumption using passive elements. However, engineering high degrees of graph connectivity—which has been achieved with good control in cold atom ensembles in optical cavities [26]—presents still a major hurdle in many of the abovementioned photonic platforms. As an exam-

ple, in planar microcavity exciton-polariton condensates the coupling strength between neighboring condensates decays exponentially with their spatial separation distance [27, 28], making the coupling beyond nearest neighbors usually negligible. That, plus the need to control each inter-condensate coupling strength makes it nigh on impossible to solve an all-to-all connected graph beyond a handful of condensate vertices. A scheme to achieve all-to-all coupling between polariton condensate modes was theoretically proposed using a fast time-modulated nonresonant laser [29]. We show that these connectivity problems can, in principle, be overcome using the minor embedding technique to the triad structure, which realizes a more experimentally friendly, on chip, strategy to simulate dynamics and emergent behaviours in all-to-all connected networks of nonlinear optical oscillators.

We focus on two measures, and compare them between non-embedded and corresponding embedded networks, to quantify the applicability of our technique. Firstly, calculate and characterize the emergence of coherence in disordered ferromagnetically connected Stuart-Landau oscillatory networks [30] with increasing coupling strength. Second, we investigate the efficiency of embedded oscillatory networks to approximate low energy solutions of the classical XY Hamiltonian through dynamical annealing [31, 32].

II. THE STUART-LANDAU MODEL

The Stuart-Landau model describes a plethora of oscillatory systems and is formally derived from the normal form of an Andronov-Hopf bifurcation. We apply this universal model to describe the dynamics of our dissipatively coupled oscillators at the graph vertices written:

$$\frac{d\psi_n}{dt} = -\left[i\omega_n + |\psi_n|^2\right]\psi_n + \sum_{m=1}^{N} J_{n,m}\psi_m \qquad (1)$$

Here, $\psi_n \in \mathbb{C}$ denotes the nth oscillator, ω_n its intrinsic frequency, and $J_{n,m}$ is the coupling strength between oscillator n and m corresponding to the weighted

edge connecting graph vertices n and m. We can re-write the Stuart-Landau model in polar coordinates with $\psi_n = \rho_n e^{i\theta_n}$ arriving at:

$$\frac{d\rho_n}{dt} = -\rho_n^3 + \sum_m J_{n,m}\rho_m \cos(\theta_m - \theta_n); \qquad (2)$$

$$\frac{d\theta_n}{dt} = \omega_n + \sum_m J_{n,m}\frac{\rho_m}{\rho_n}\sin(\theta_m - \theta_n). \qquad (3)$$

If the amplitudes of the oscillators are set as equal $\rho_n = \rho_0$, and with zero detuning $\omega_n = 0$, then Equation 3 describes the generalized *Kuramoto model* [33, 34]. The fixed points of a Kuramoto network are described by the minima of the following Lyapunov potential [30],

$$\mathcal{L} = -\sum_{n,m} J_{n,m} \cos(\theta_n - \theta_m), \qquad (4)$$

which is the same as the well known XY Hamiltonian. Therefore, the phases θ_n in a Kuramoto network experience a gradient descent towards local minima of the XY Hamiltonian $\dot{\theta}_n = -\partial\mathcal{L}/\partial\theta_n$. In this respect, the phasors $\mathbf{s}_n = [\cos(\theta_n), \sin(\theta_n)]^{\mathrm{T}}$ play the role of two-dimensional classical spins which experience phase space flow towards these minima. This is in a similar spirit to Ising machines which undergo quantum or classical annealing into the ground state of some target Ising Hamiltonian [35]. In this sense, $J_{n,m} > 0$ are said to be ferromagnetic links (in-phase coupling) and $J_{n,m} < 0$ are antiferromagnetic links (anti-phase coupling).

Surprisingly, even with coupling induced amplitude inhomogeneity $\rho_n \neq \rho_m$ Stuart-Landau networks have displayed impressive results in approximating the global minima of the XY Hamiltonian in dense networks [32]. In Sec. IV B we will characterize the quality of using a minor embedding technique to simulate densely connected Stuart-Landau networks by comparing their performance in approximating low energy solutions of the XY Hamiltonian against corresponding non-embedded networks.

III. MINOR EMBEDDING

A. Triad Graph

In the process of creating a triad graph, we must first consider the undirected complete graph (all-to-all connected graph) of N vertices K_N, with vertex set: $V(K_N)$ and edge set: $J(K_N)$. Each vertex V_n is assigned an index n and each edge symmetrically connecting two distinct vertices V_n and V_m is denoted $J_{n,m} = J_{m,n}$. Through the process of minor embedding, K_N is mapped to the triad graph K_N^{emb} [shown for K_5 in Figure 1(a,b)] by expanding each vertex $V_n \in V(K_N)$ to a chain of uniform coupled vertices of length $N-1$, with intra-chain edge weights set to,

$$J^{\mathrm{intra}} = J_c > 0, \qquad \text{(colored edges).} \qquad (5)$$

Each vertex of the chain is adjacent to a single vertex of a another chain with inter-chain edge weights,

$$J_{n,m}^{\mathrm{inter}} = J_{n,m}, \quad \forall\, J_{n,m} \in J(K_N), \quad \text{(black edges).} \qquad (6)$$

Additional description can be found in [36].

Physically, $J_c > 0$ gives precedence to in-phase locking between oscillators within each chain, which—in the context of the XY Hamiltonians—can be regarded as a ferromagnetic (FM) type coupling. The aim of FM coupling is to minimize the deviation between oscillators across each chain, in order to better simulate the dynamics of the complete graph K_N [8]. In other words, the red vertex in the complete graph [red oscillator ψ_1 in Figure 1(a)] is represented by the average amplitude and phase of the oscillators in the red chain of the triad [see grey solid box in Figure 1(b)]. Notice that the number of black edges in the complete graph is the same as in the triad graph.

In this study, we will work close to the bifurcation threshold of the system separating the attenuated state $\rho_n = 0$ from the oscillatory state $\rho_n \neq 0$, and are thus interested only in the phases of the oscillators whose average in each colored chain is written,

$$\bar{\theta}_n = \frac{1}{N-1} \sum_{n' \in \mathrm{chain}}^{N-1} \theta_{n,n'}. \qquad (7)$$

We will refer to this phase averaging as *unembedding* the triad graph [37, 38]. That is, the averaged phases $\bar{\theta}_n$ of the triad graph have been unembedded back to the vertices of the original complete graph.

Where the triad structure in Figure 1(b) is the hardware layout for investigating the minor embedding of complete graphs, it can be easier to picture the mapping process as the mathematical layout shown in Figure 1(c), where each vertex of K_N is expanded to a chain of length $N-1$ about its original vertex site, such that the adjacency of the hardware layout [Figure 1(b)] and mathematical layout [Figure 1(c)] are equivalent.

We also consider the addition of an intra-chain edge between the first and last vertex of each chain [Figure 1(d)], thus "looping" them, such that the looped graph has a uniform degree of connectivity. Although this is more difficult to realize experimentally in most platforms, we will compare results between unlooped and looped chains at minimising the XY Hamiltonian, and elucidate on how this more "symmetric" connectivity affects the performance of the triad graph.

B. XY Energy Extraction

As mentioned above, each vertex of the complete graph K_N is associated with a complex valued number ψ_n containing information on the state the nth oscillator. We define the state vector of the graph as $\boldsymbol{\psi} = [\psi_1, \psi_2, \ldots \psi_N]^{\mathrm{T}}$ and its corresponding phase vector $\boldsymbol{\theta} = [\theta_1, \theta_2, \ldots \theta_N]^{\mathrm{T}}$. The energy of the graph K_N is

calculated from the XY Hamiltonian written,

$$H_{XY} = -\sum_{n,m}^{N} J_{n,m} \cos(\theta_n - \theta_m). \tag{8}$$

On the other hand, the energy of the triad graph can follow two methods. The first one defines the energy of the unembedded triad in the same way as Equation 8 but with the average phases across the chains $\bar{\theta}_n$,

$$H_{XY}^{\text{unemb}} = -\sum_{n,m}^{N} J_{n,m} \cos(\bar{\theta}_n - \bar{\theta}_m). \tag{9}$$

We refer to this as the *unembedded energy* of the triad.

The other method directly uses the relative phase $\Delta\theta_{n,m}^{\text{inter}}$ between all pairs of oscillators still "embedded" in the triad graph connected by a black inter-chain edge as depicted by the grey dashed boxes in Figure 1(a,b). We will refer to this as the *embedded energy* of the triad graph written,

$$H_{XY}^{\text{emb}} = -\sum_{n,m}^{N} J_{n,m} \cos(\Delta\theta_{n,m}^{\text{inter}}). \tag{10}$$

Note that when $J_c = 0$ then minimising H_{XY}^{emb} is trivial since the graph forms just a set of N individual oscillator pairs connected by $J_{n,m}$.
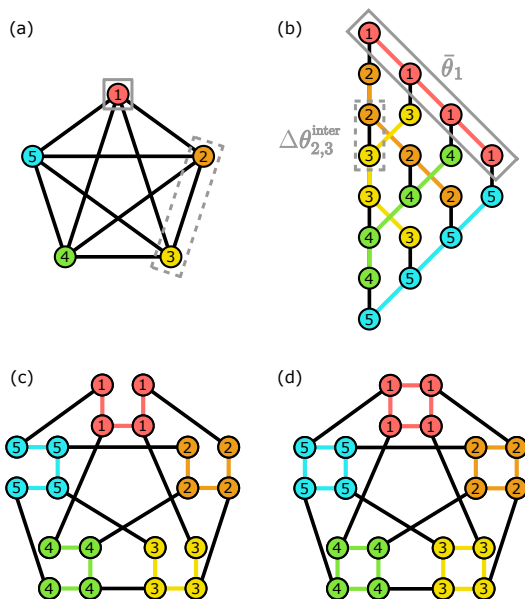

FIG. 1. (a) K_5 graph mapped through minor embedding to (b) the K_5^{emb} triad graph, (c) the mathematical layout of K_5^{emb} and (d) when including N additional edges to loop the chains. In (b-d), the FM chain couplings are shown by colored edges $J^{\text{intra}} = J_c$ and the encoded coupling strength of K_5 are shown by black edges, such that $J_{n,m}^{\text{inter}} = J_{n,m}$. The grey solid and dashed boxes overlayed on (a,b) demonstrate two possible phase extraction methods for the unembedded and embedded XY energies from the triad graph respectively.

IV. RESULTS

A. Coherence Properties

Here, we numerically investigate and compare the phase coherence properties (i.e., the ability to synchronize in-phase) in the oscillator network dynamics between the complete graph and the triad graph. We consider a complete FM graph where each oscillator is coupled equally to all the others with coupling strength $J_{n,m} = J > 0$. The frequencies ω_n are randomly chosen from a normal distribution with density $g(\omega)$ of mean $\bar{\omega}$ and standard deviation σ. Naturally, we can always go into a rotating reference frame with frequency $\bar{\omega}$ and therefore we can set $\bar{\omega} = 0$ throughout our study without any loss of generality. We will use dimensionless units for all parameters and variables and fix $\sigma = 1$ in this section. We point out that the oscillator coupling matrix $\mathbf{J} = (J_{n,m}) \in \mathbb{R}^{M \times M}$ has always at least one positive eigenvalue for all graphs considered throughout the paper which means that the trivial $\rho_n = 0$ solution is never stable. This means that the phases $\theta_n(t)$ are well defined at all times when calculating the dynamics of Equation 1.

To understand the emergent coherence properties of the network it is useful to define a phase order parameter, commonly used in analysis of such networks [30], to capture the degree of phase coherence between the oscillators. For the complete graph it is written,

$$r_{\text{complete}} = \frac{1}{N} \left| \sum_{n=1}^{N} e^{i\theta_n} \right|. \tag{11}$$

If all the oscillators have the same phase $\theta_n = \theta_m$ then $r_{\text{complete}} = 1$, and in the limit of infinitely many uniform-randomly distributed phases on the interval $[0, 2\pi)$ one has $r_{\text{complete}} = 0$. We have checked that the special case of $r_{\text{complete}} = 0$ where half of the oscillators are $\theta_n = 0$ and other half $\theta_n = \pi$ (i.e., anti-phase ordering) does not appear in our results.

We numerically integrate Equation 1 from $t = 0 \rightarrow T \gg J^{-1}, J_c^{-1}$ and calculate the average coherence $\langle r_{\text{complete}} \rangle$ at the final time $t = T$ over 160 random realizations of ω_n and initial conditions (i.e., Monte Carlo sampling). We then repeat our calculation over a range of coupling strengths J [see Figure 2(a)] observing a gradual transition from an incoherent state to a coherent state with increasing coupling strength. This is reminiscent of the coherence bifurcation in Kuramoto networks [30, 34]. There, all phase oscillators are in an incoherent state $r_{\text{complete}} = 0$ below some critical coupling strength J_{crit} defined in the limit $N \rightarrow \infty$. As J is increased through and above J_{crit}, the system reaches a partially synchronized state $r_{\text{complete}} > 0$, where oscillators at the centre of $g(0)$ are synchronized while those at the tails of the distribution remain in an incoherent state such that the system is split in two dynamical groups [39]. As J is increased further, more oscillators join the synchronized group until the entire system becomes coherent [33, 40],
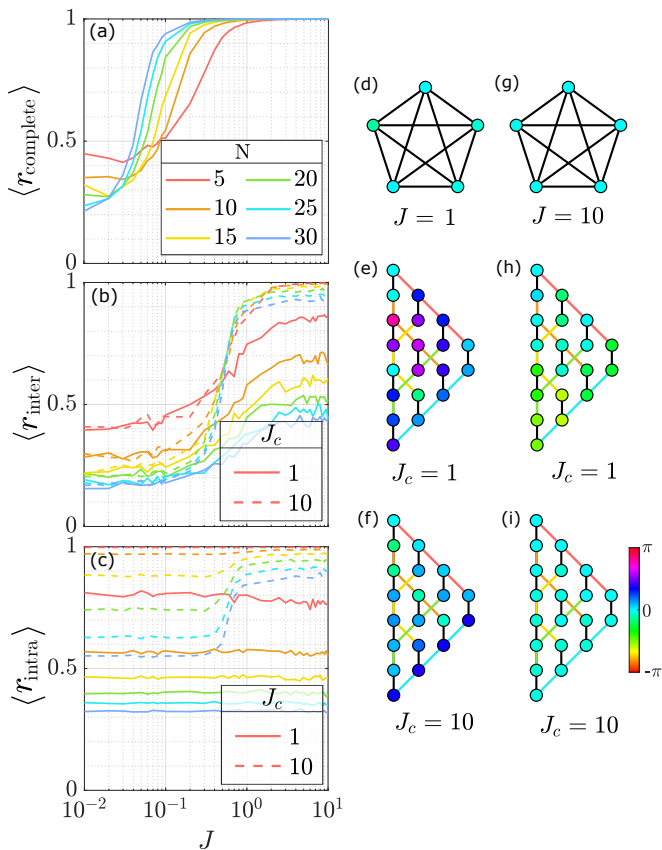
the triad,

$$r_{\text{intra}} = \frac{1}{N} \sum_{n=1}^{N} \underbrace{\frac{1}{N-1} \left| \sum_{n' \in \text{chain}}^{N-1} e^{i\theta_{n,n'}} \right|}_{r_n^{\text{intra}}}. \qquad (13)$$

For more details, please see Figure 8 in section A. Just like for the complete graph, we average the coherences of the triad over 160 random samples of the dynamics denoted by $\langle . \rangle$.

Considering two different orders of the scaling parameter $J_c = \{1, 10\}$, we investigate how the triad graph's coherence properties relate to the complete graph (going to lower and larger orders of J_c did not qualitatively change the findings). Note that the frequencies ω_n are randomly drawn from $g(\omega)$ for all oscillators in the triad which represents experimental reality (i.e., we do not associate a single random frequency across each chain). As expected, when J_c is small the inter- and intra-chain coherences in Figure 2(b,c) show poor coherence with weak dependence on J. When J_c is large we instead observe a fast inter-chain coherence transition in Figure 2(b). This indicates that the triad graph managed to represent the embedded complete graph dynamics within $J/J_c < 0.1$ which gives a figure of merit for the design requirements of possible triad graph platforms. Interestingly, in Figure 2(b) for large J the coherence is smaller in large graphs. This can be attributed to the fact that the chains within the triad graph need themselves to be coherent, $r_{\text{intra}} \approx 1$, in order to represent the embedded complete graph. But longer chains struggle more to settle on a phase and achieve good coherence as can be seen in Figure 2(c), such that the larger graphs in general require a stronger FM coupling strength in order to build coherence.

As both J and J_c increase, both inter and intra-chain coherences converge to unity and all oscillators synchronize. In Figure 2(d-i) we show example simulations of varying coupling strength where the vertex colors represent the steady state oscillator phases. The effect of looping the chains like shown in Figure 1(d) is found to have little effect on the coherence properties of the system (see Figure 9).

To better understand the quality of the triad graph as a simulator for the phase dynamics of the complete graph we calculate the root mean square error (RMSE) between the phases in the complete graph θ_n and their corresponding representations in the triad graph $\bar{\theta}_n$ as a function of J_c. For brevity, we use the same set of randomly sampled detunings ω_n with strength σ, and same random initial conditions $\psi_n(t = 0)$ across all calculations in order to quantify the similarity between the complete and the triad graph. We define a gauge-invariant

FIG. 2. Coherence of (a) $\langle r_{\text{complete}} \rangle$ for uniform FM coupled complete graphs with coupling strength J, (b) $\langle r_{\text{inter}} \rangle$ and (c) $\langle r_{\text{intra}} \rangle$ for the corresponding triad graphs. All results are averaged over 160 instances of ω_n and random initial conditions. Plots (a-c) all share the same x-axis. Example steady state phases of $N = 5$ oscillators in the (d,g) complete and triad structures with (e,h) $J_c = 1$ and (f,i) $J_c = 10$ for a single instance. (d-f) $J = 1$ and (g-i) $J = 10$, where the phases are indicated by vertex color.

as we observe with the Stuart-Landau model. Finite size effects can also be clearly observed in Figure 2(a) when changing the number of oscillators N. Notably, larger coupling strengths are needed to synchronize smaller networks. We also point out that the presence of finite coherence values as $J \to 0$ arises from these finite size effects which gradually decrease as N becomes larger.

We now move onto the triad graph. Similar to Equation 11, we can define coherence order parameters for the unembedded (averaged) phases of the triad graph,

$$r_{\text{inter}} = \frac{1}{N} \left| \sum_{n=1}^{N} e^{i\bar{\theta}_n} \right|, \qquad (12)$$

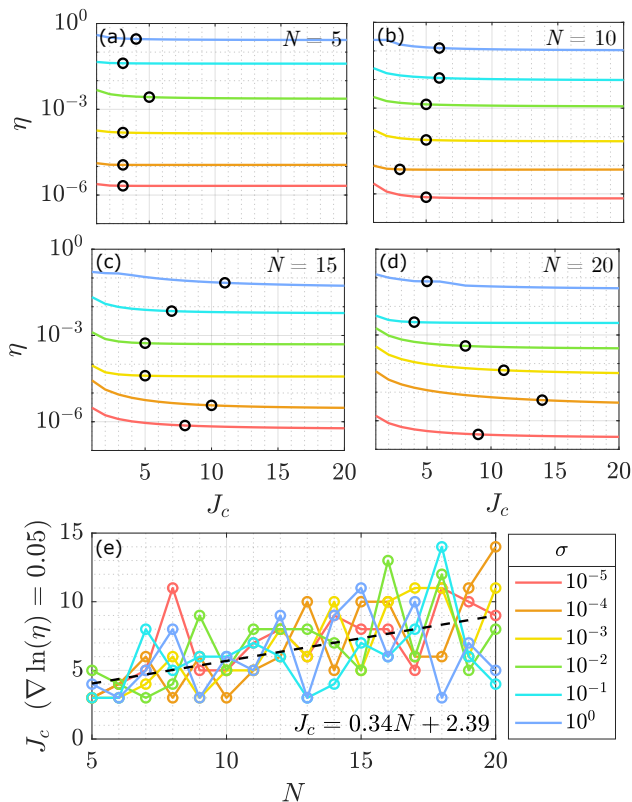and for the average phase coherence within each chain of

FIG. 3. RMSE between the complete and triad graph phase dynamics for (a) $N = 5$, (b) $N = 10$, (c) $N = 15$ and (d) $N = 20$ oscillators over a range of J_c and σ. The black circles indicate the value of J_c where the gradient of $\ln(\eta)$ surpasses 0.05. These points are collated in (e) and are plot as a function of N, where a linear fit is shown by a black dashed line following $J_c = 0.34N + 2.39$.

RMSE measure as

$$\eta = \frac{1}{N(N-1)T} \left[\sum_{n<m} \sum_{t=1}^{T} \left[\cos\left(\theta_{nm}(t)\right) - \cos(\bar{\theta}_{nm}(t)) \right]^2 \right. $$
$$\left. + \left[\sin\left(\theta_{nm}(t)\right) - \sin(\bar{\theta}_{nm}(t)) \right]^2 \right]^{\frac{1}{2}} \tag{14}$$

where $\theta_{nm} = \theta_n - \theta_m$ for the complete graph phases and $\bar{\theta}_{nm} = \bar{\theta}_n - \bar{\theta}_m$ for the representative triad graph phases. The RMSE is calculated only for the last 200 timesteps of each simulation in order to skip any transient effects that might be strongly dissimilar at early times between the complete and the triad graph.

In Figure 3(a-d), we plot the RMSE with $N = 5$, 10, 15 and 20 respectively, which show that the RMSE converges towards a minimum with increasing J_c, where we have marked with black circles the values of J_c where the gradient of $\ln(\eta)$ surpasses 0.05.

The corresponding J_c values where $\nabla \ln(\eta) = 0.05$ are collated in Figure 3(e), showing that the optimum value of J_c increases with the number of oscillators and, in-

terestingly, appears to be independent of the strength of detuning σ. We apply a linear fit to this data, shown by the black dashed line, with $J_c = 0.34N + 2.39$ which gives an estimation of what value of intra-chain coupling strength in the triad J_c is needed in order to simulate the dynamics of the complete graph.

B. XY Energy Minimization

In this section we investigate the feasibility in using the minor embedding technique on complete graphs of Stuart-Landau oscillators to optimize the XY Hamiltonian. We compare the unembedded and embedded complete graph XY energies extracted from the triad structure [Equation 9,10] to the ground state of the XY Hamiltonian, as calculated using the basin hopping optimization method [41]. Here we measure the performance of the Stuart-Landau system through the normalized difference in the extracted XY energy from solving the dynamics of the triad graph of Stuart-Landau oscillators E_{SL} compared to the complete graph XY energy solved using the basin hopping method E_{BH},

$$\text{Error} = \frac{E_{BH} - E_{SL}}{E_{BH}}. \tag{15}$$

The basin hopping algorithm is time consuming but a highly accurate optimization algorithm that serves as a good reference for the energies found by the solving the dynamics of triad embedded Stuart-Landau networks. Previous studies on complete graphs (i.e., no embedding techniques) have shown very good performance from numerically solving the dynamics of Stuart-Landau networks as compared to the basin hopping algorithm [32]. For completeness, we provide evidence in section B that the Stuart-Landau network indeed outperforms commercial optimizers, and also direct integration of the Kuramoto model, in finding low energy solutions of the XY Hamiltonian. Throughout this section, the performance is obtained by averaging over 160 unique complete graphs with weights randomly selected from a uniform distribution $J_{n,m} \in [-1, 1]$ (there is no qualitative difference in using a normal distribution of same variance).

To find the optimum embedding parameter J_c, we first consider a graph size of $N = 10$ in Figure 4. In Figure 4(a) we show the system performance for $\sigma = 0$ and scanning across the embedding parameter J_c. The error of the extracted XY energies reduces as J_c is increased, where the unembedded XY energy converges to zero faster than the embedded energy, with a reduction in error for both methods when the triad chains are looped. This result is to be expected, as larger values of J_c reduce the distribution of oscillator amplitude and phase across each triad chain, achieving a better representation of the complete graph in corroboration with Figure 2(b). This is seen in Figure 4(b) where the phase dynamics $\theta_n(t)$ of the $N(N-1) = 90$ triad graph oscillators split into
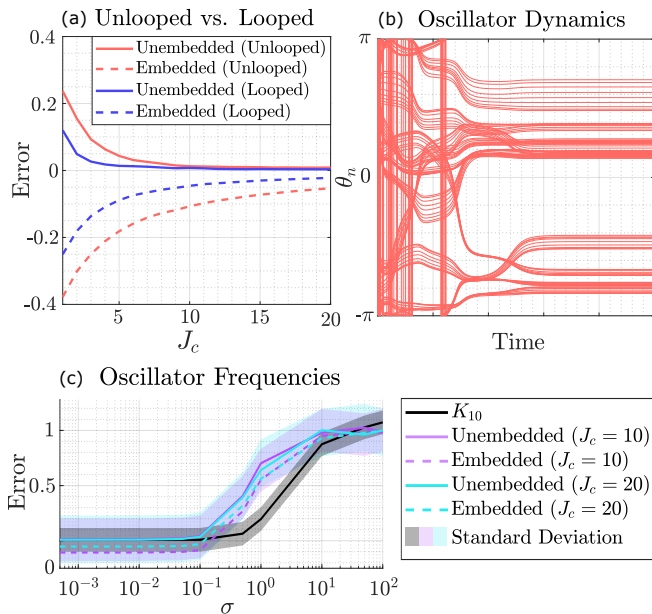
FIG. 4. (a) Error between the triad embedded Stuart-Landau model and the basin hopping method in minimising the XY Hamiltonian on a randomly connected complete graph with $N = 10$ vertices and $\sigma = 0$. (b) Example phase dynamics of the triad embedded oscillators for a single random graph with $J_c = 10$, indicating clustering of the phases in different chains. (c) Performance of the system for increasing strength in oscillator frequencies ω_n for unlooped triad graphs with $J_c = 10$ (purple), $J_c = 20$ (cyan) and the complete K_{10} graph (black) for reference, with translucent surfaces to represent the standard deviation in error of the unembedded energies. Results in (a,c) are averaged over 160 random graphs and initial conditions and, in the case of (c), for random oscillator energies ω_n.

10 moving paths, with each path representing a different triad chain.

Interestingly, looping the triad chains in the considered case of $N = 10$ oscillators is found to reduce the phase variation within each chain (see Figure 9), achieving lower error (see Figure 4). However, for larger N the error starts increasing (see Figure 5 in the Appendix) which we discuss in more detail at a later stage. We point out that the negative error for the embedded XY energy stems from the fact that $\min[H_{XY}^{\mathrm{emb}}] < \min[H_{XY}]$ when $J_c \to 0$. In this limit, the triad graph breaks into N pair-coupled oscillators (only black edges remain) and the sum of their XY energies is trivially minimized by simply setting the relative phase in each pair to $\Delta\theta_{n,m} = 0, \pi$ for positive and negative couplings, respectively.

In Figure 4(c) we show the performance of Stuart-Landau networks in dynamically finding a good XY energy when including random oscillator frequencies ω_n, normally distributed with standard deviation σ. Here, we focus on unlooped triad graphs with $J_c = 10$ and $J_c = 20$. As an additional reference, we also plot the performance of the Stuart-Landau oscillators in the original complete K_{10} graph (black line). As expected, the fre-
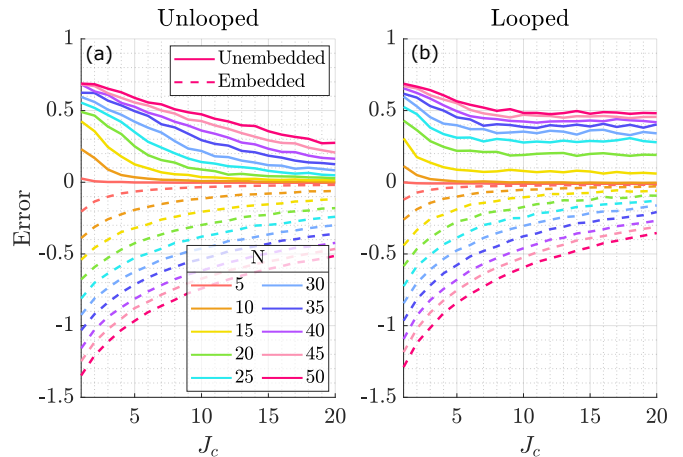

FIG. 5. XY energy error from the triad structure of Stuart-Landau oscillators compared to the complete graph XY energy solved using the basin hopping method for (a) unlooped and (b) looped triad chains with $N = 5$ to 50, averaged over 160 random graphs and $\sigma = 0$.

quencies ω_n lead to desynchronization and fast increase in error with increasing σ, and the network steady state is lost with no well-defined phase relation that can enter into the XY Hamiltonian. This increase in error in the Stuart-Landau networks occurs for $\sigma \gtrsim \frac{1}{10}$ which is in qualitative agreement with coherence transition in Figure 2(b).

Lastly, we show the performance of the triad graph as a function of both the problem (i.e., network) size N and J_c in Figure 5. As before, the error converges to zero with increasing J_c with better performance for the unembedded XY energy. As expected, larger networks struggle to find the correct (global) XY energy minimum and instead stabilize into the growing number of local minima. Interstingly, in Figure 5(b), when the chains are looped the unembedded XY energy error plateaus such that beyond $J_c = 10$, the embedded energy does not noticeably change and the benefit of looping the chains is only apparent for $N \leq 10$. This puzzling behaviour implies that looping the chains in the triad graph has generated a new family of stable attractors which do not correlate with the minima of the XY Hamiltonian. Such attractors could belong to twisted states in the chains which appear in sparse networks [42], which we explore in the following section.

C. Twisted States

Twisted states in oscillatory networks are characterized by a winding number, ℓ, denoting integer multiples of 2π phase winding about a network of FM coupled oscillators [42]. Typically, these states appear in looped networks (where the first and last oscillators in a chain are connected) with sparse connectivity up to the first few nearest neighbors. Although an interesting nontriv-

ial state, this family of attractors is however detrimental to the performance of the looped triad graph to find good XY energy minima. For the triad to best represent the complete graph, the FM chains in the triad should have all sites following same phase dynamics (or as similar as possible) in order to represent the dynamics of a single oscillator in the complete graph. Appearance of a vortex phase gradient in the looped triad chains is clearly detrimental to this requirement.

Networks of N identical Kuramoto oscillators have recently been studied with unit FM coupling to $\mu(N-1)$ nearest neighbors [42], where $\mu > 0.75$ guarantees that all oscillators will converge to a synchronized in-phase configuration with $\ell = 0$. Below this threshold however, the loop of oscillators exhibit a constant relative phase difference between nearest neighbors of $2\pi\ell/N$, where $\ell \neq 0$. These solutions are known as *twisted states*.

To explore the occurrence of twisted states in the Stuart-Landau model, we create networks of N identical oscillators ($\sigma = 0$) in loops (just like a single looped chain of a triad graph) with unitary FM coupling and plot the distribution of different winding numbers ℓ that appear in the system over 1000 unique realizations as a function of nearest neighbor connectivity and varying N in Figure 6(a-d). Remarkably, we find that twisted states appear frequently in our simulations. For larger N, the spread in ℓ is greater, but reduces quickly as the number of nearest neighbor connections increases. When $N = 20$ for example, we observe $|\ell| = 0, 1, 2$ for first nearest neighbor coupling, but this range decreases to $|\ell| = 0, 1$ when second nearest neighbor coupling is introduced, as depicted in Figure 6(e-i) where the oscillators (circles) have unit FM coupling following the black graph edges and their steady-state phases are shown by their color. In this analysis, $|\ell| = 2$ occurred in 0.1% of the cases for $N = 20$ with first nearest neighbor connectivity, so it is very unlikely to observe a phase winding greater than 2π in a smaller chain. This is the likely reason that looped-chain triad graphs do not converge to zero energy error in Figure 5(b), but instead plateau to a larger error that grows in value with increasing N. As non-zero winding numbers in Stuart-Landau chains grows in probability with N, we emphasize that it is important to sample the system over many realizations starting with different random initial conditions in order to increase the chances of finding an XY energy closest to the XY ground state.

D. Dynamic Pumping

The presence of random couplings induces an amplitude inhomogeneity in the Stuart-Landau network $\rho_n \neq \rho_m$, meaning its fixed points will, in general, not coincide exactly to the minima of the XY model. As a possible improvement to achieve amplitude homogeneity [32, 43], we investigate the addition of a dynamic
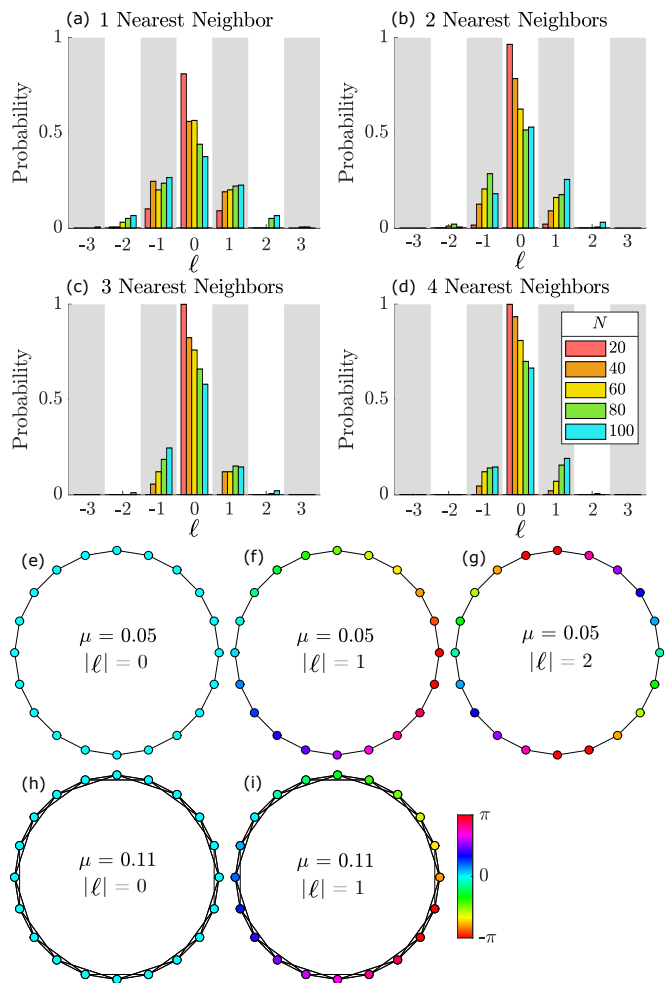

FIG. 6. Distribution in winding number ℓ extracted from a continuous chain of Stuart-Landau oscillators with (a-d) 1-4 nearest neighbor couplings with unitary strength ($J = 1$) respectively for $N = 20, 40, 60, 80$ and 100 shown in red, orange, yellow, green and blue bars respectively, over 1000 unique realizations. For $N = 20$, an example of each stable phase solution is shown in graph format with (e-g) 1 and (h,i) 2 nearest neighbor connections, showing all observed values of $|\ell|$ over 1000 realizations.

pumping mechanism that feeds back the amplitude of each oscillator at each step in numerical integration in order to adjust the gain of each node respectively. To explore this feedback mechanism, we adjust Equation 1 slightly to follow:

$$\frac{d\psi_n}{dt} = [P_n(t) - i\omega_n - |\psi_n|^2]\psi_n + \sum_{m=1}^{N} J_{n,m}\psi_m. \quad (16)$$

Here, $P_n(t)$ is the pumping rate of oscillator ψ_n where initially all oscillators are injected equally with $P_n(0) = 0$ for all n. In terms of exciton-polariton condensates [11, 16], the pumps represent an arrangement of spatially modulated nonresonant excitation beams. After the initial pumping in the first time step of integration,
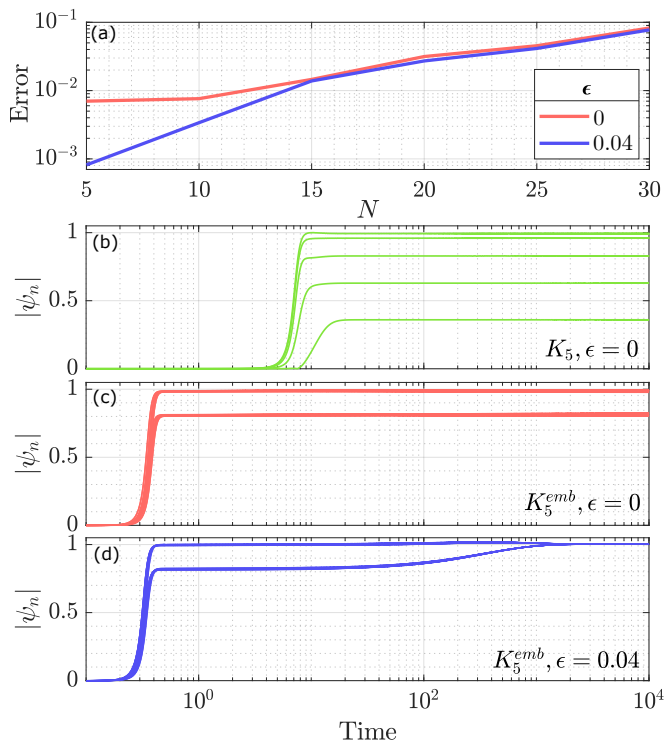
FIG. 7. (a) Unembedded energy error of randomly connected triad graphs with (red) $\epsilon = 0$ and (blue) $\epsilon = 0.04$ with $J_c = 20$ over a range of N, averaged over 100 unique random graphs realizations. Oscillator amplitude dynamics for (b) a randomly connected K_5 graph with $\epsilon = 0$, and the corresponding $J_c = 20$ triad graph with (c) $\epsilon = 0$ and (d) $\epsilon = 0.04$, with amplitudes normalized to $\max |\psi_n|$ and $\rho_t = \max |\psi_n|$. The same x-scale is used for panels (b-d).

we apply a feedback mechanism to balance the occupation of each oscillator, following:

$$\frac{dP_n}{dt} = \epsilon \left[\rho_t - \rho_n(t)\right] \tag{17}$$

where ϵ controls the rate of change of P_n, ρ_t is the target amplitude of the oscillators. We numerically integrate Equations 16 and 17 for 100 unique randomly-connected complete graphs and corresponding triad graphs with varying N, $J_c = 20$, and for $\epsilon = 0$ and $\epsilon = 0.04$. The resulting performance, and amplitude dynamics for a single instance of the network is shown in Figure 7.

We do indeed see a considerable drop in error for smaller networks when the feedback is present. However, for larger networks the error is dominated by the approximative nature of the embedding procedure and the role of feedback becomes less important. It could be possible to design a more complex feedback procedure which not only eliminates amplitude inhomogeneity but also helps balance the phases in each chain of the triad graph, but this is beyond the scope of the current study. Note, due to the large intra-chain couplings J_c in the triad graph, the oscillator amplitudes reach saturation an order of magnitude sooner than for the equivalent

complete graph.

V. CONCLUSIONS

We have demonstrated that the dynamics of an random all-to-all coupled Stuart-Landau oscillator network can be approximated using a minor embedding technique, regularly applied in the design of quantum computing platforms. Here, a complete (dense) graph is embedded into a sparse triad graph defined by a single embedding parameter J_c. We show that the steady-state phases in the embedded Stuart-Landau oscillator network correspond to good approximation of the optimal solutions in the corresponding graph XY Hamiltonian, achieving good performance by simply adjusting its embedding parameter. The results are compared against the standard complete graph Stuart-Landau oscillator dynamics, and the basin hopping method.

The convergence of the minor embedded graph dynamics to that of the complete graph offers up the triad structure as a potential testbed for mapping out dense graph problems to continuous-phase coupled oscillator systems where fully-controllable all-to-all couplings are not practicable (such as polariton condensates, photonic condensates, and coupled laser arrays). This opens perspectives on designing analogue computing hardware aimed at heuristically solving dense graphs problems (such as optimising the XY Hamiltonian) across a wide range of platforms in a similar spirit to quantum computing platforms. Optical systems might hold a particularly strong promise in this regards since their GHz operation rates can provide rapid sampling of the objective function energy landscape that can serve as good trial points for more sophisticated optimizers.

Appendix A: Coherence

1. Definitions

In the main text we extract the coherence across all oscillators in the complete graph r_{complete}, the coherence across the average phases of the chains r_{inter} and the average coherence across each chain r_{intra}. All three parameters are defined alongside a schematic in Figure 8. Here, θ_n is the phase of oscillator n in the complete graph, $\theta_{n_{n'}}^{\text{intra}}$ is the phase of the n'^{th} oscillator in triad chain n and $\bar{\theta}_n$ is the average phase over the $N-1$ oscillators in chain n.

2. Looping Triad Chains

In addition to the unlooped triad representation of the uniform ferromagnetic (FM) complete graph in the main text, we also consider the effect of looping the triad chains
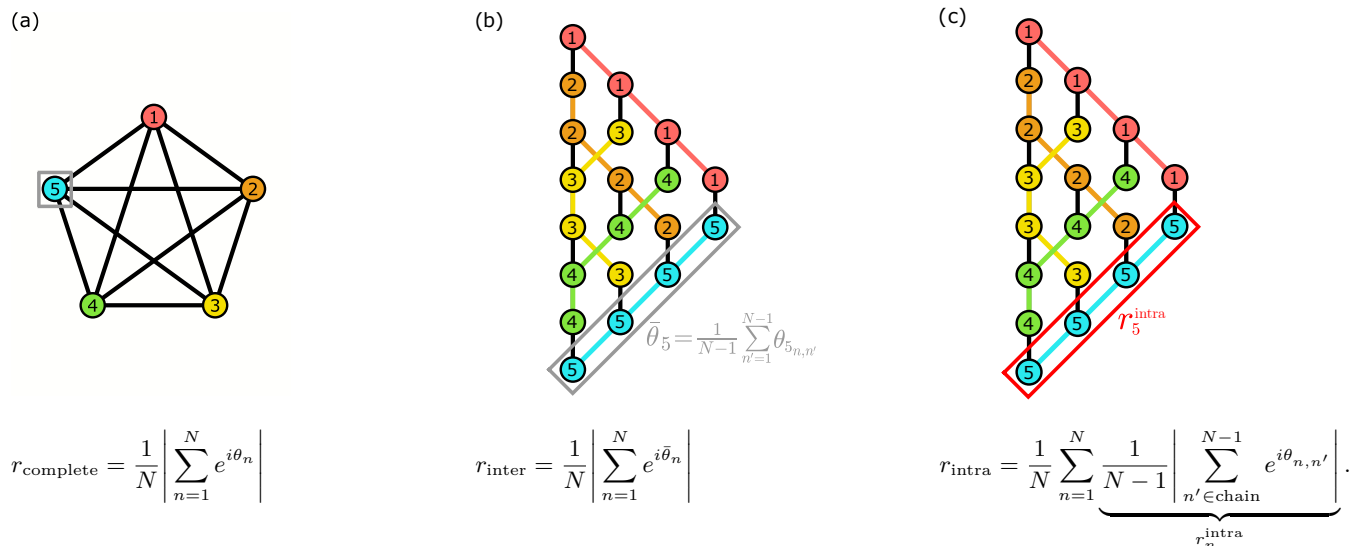
FIG. 8. (a) Coherence extracted over all oscillators in the complete graph, (b) the unembedded triad coherence between the N average chain phases, plus (c) the average chain coherence. All schematics represent the K_5 and K_5^{emb} graphs with the grey boxes in (a,b) and red box in (c) representing the extraction of the average phase and coherence across chain 5 respectively.

$$r_{\text{complete}} = \frac{1}{N} \left| \sum_{n=1}^{N} e^{i\theta_n} \right|$$

$$\bar{\theta}_5 = \frac{1}{N-1} \sum_{n'=1}^{N-1} \theta_{5_{n,n'}}$$

$$r_{\text{inter}} = \frac{1}{N} \left| \sum_{n=1}^{N} e^{i\bar{\theta}_n} \right|$$

$$r_{\text{intra}} = \frac{1}{N} \sum_{n=1}^{N} \underbrace{\frac{1}{N-1} \left| \sum_{n' \in \text{chain}}^{N-1} e^{i\theta_{n,n'}} \right|}_{r_n^{\text{intra}}}.$$
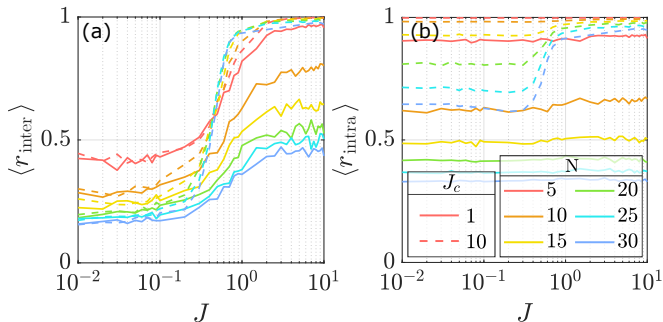

FIG. 9. Coherence (a) $\langle r_{\text{inter}} \rangle$ and (b) $\langle r_{\text{intra}} \rangle$ of triad graphs corresponding to uniform FM complete graphs with looped chains and $J_c = 1$ and 10. All scanned over a range of coupling strengths J and averaged over 160 instances with standard deviation in oscillator frequencies $\sigma = 1$.

on the coherence of the system under the same conditions as the unlooped case [9]. When the minor embedded chains are looped, all oscillators are symmetrically coupled and thus the triad graph coherence is higher for the same coupling strength compared to the unlooped equivalent, as the edge effects of the unlooped chain coherence are eliminated. For $J_c = 1$, r_{inter} and r_{intra} remain at a low coherence as the encoded complete graph weights are not dominant in the system. For $J_c = 10$, there is a coherence build up with increasing J, indicating that the triad coherence dynamics represent the complete graph for large J_c.

Appendix B: Benchmarking Stuart-Landau networks in finding low energy XY solutions

1. Stuart-Landau networks against global optimizers using trust-region methods

Here we will benchmark the performance of dense Stuart-Landau (SL) networks against commercially available global optimizers. We have applied the *Basin Hopping* (BH) algorithm from the Python SciPy library as a benchmark in the main manuscript. However, we point out that we are benchmarking dense graphs meaning that a $N = 50$ vertex graph has $N(N-1) = 2450$ weighted edges to be optimized. The reason we limit ourselves to $N = 50$ vertices in this study is because running the BH algorithm with 1000 iterations (for good convergence) for larger graphs on a single 2.6 GHz Intel Sandybridge processor (components of the IRIDIS 4 supercomputer at University of Southampton) exceeded 100 hours.

As a result, to investigate graphs of $N > 50$, instead of using the BH algorithm we have decided to use the speedier and commercially available global optimizer GlobalSearch [44] (GS) from the Global Optimization Toolbox [45] of Matlab$^{\text{TM}}$. This algorithm uses a scatter search method to generate feasible trial points which are then evaluated using a chosen optimizer method to find multiple local minima. The GS algorithm then iteratively analyses points that converge using a score function which updates on-the-fly and rejects those points that are unlikely to improve the best minimum found so far. We have decided to use two well known optimization methods for the GS algorithm. **(1)** The *trust region* method since we can easily compute both the gradient and the Hessian matrix of the XY Hamiltonian (i.e., the objective function) making it quite fast and accurate and thus
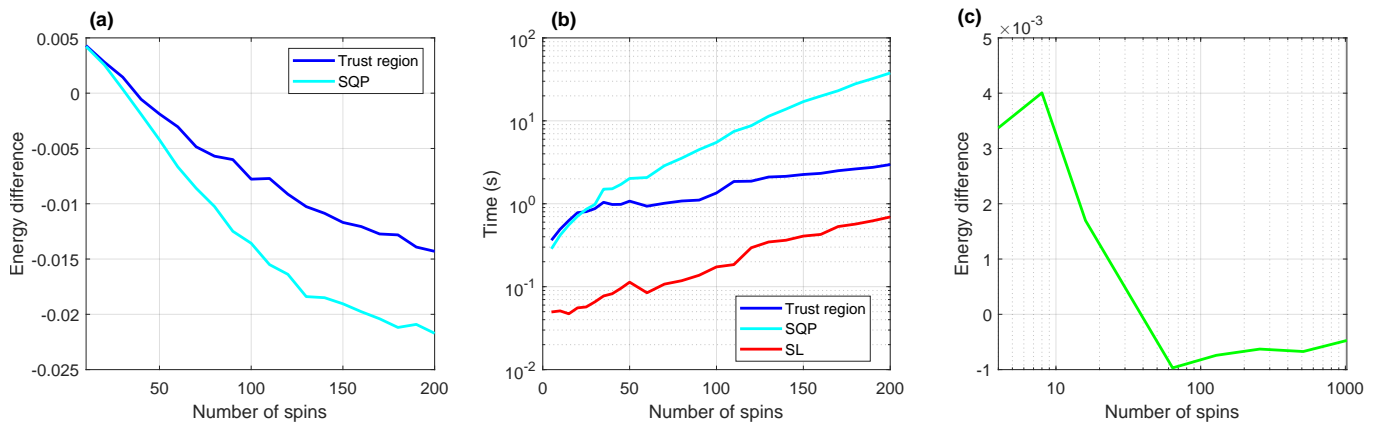
FIG. 10. (a) Average energy difference between the GS algorithm and the SL model according to Eq. (B1) with the GS algorithm using two different optimizer approaches, trust region and SQP. The SL model outperforms the GS algorithm around $N \approx 30$ spins. (b) Time taken for different methods to arrive at an answer for the XY energy. (c) Energy difference between the KM and the SL model [i.e., E_{GS} is replaced with E_{KM} in Eq. (B1)]. The SL model outperforms the KM model in finding low energy values to the XY Hamiltonian at around $N \approx 30$.

an appropriate choice. **(2)** The *sequential quadratic programming* (SQP) gradient descent method since it also benefits from knowing the gradient of the objective function. Our search region is bounded on $\theta_n \in [-4, 4]$ which is taken larger than the periodic range $[-\pi, \pi]$ in order to more efficiently find minima that might be close to values around $\theta_n = \pm\pi$. All other options of the GS algorithm were set to default as they did not considerably improve the efficiency of the optimizer.

Just like in the main manuscript, we quantify the performance between the SL model and the GS algorithm using the ratio of their energy difference,

$$\text{Energy Difference} = \frac{E_{\mathrm{GS}} - E_{\mathrm{SL}}}{2E_{\mathrm{GS}}}. \qquad (B1)$$

The factor $1/2$ is added so that if $E_{\mathrm{SL}} = -E_{\mathrm{GS}}$ then the difference is exactly unity. Our results are presented in 10(a) where we have averaged over 1000 random dense graphs with weights sampled from the interval $J_{n,m} \in [-1, 1]$ going up to $N = 200$ spins. Amazingly, even after supplying knowledge of the gradient and the Hessian of the objective function (H_{XY} in main manuscript) the SL model starts outperforming the GS algorithm around $N \approx 30$ spins. We also show in 10(b) the time taken to iterate the SL model using an explicit Runge-Kutta (4,5) method until it converged to a steady state (red line), and the time it took the trust region (blue line) and gradient descent (cyan line) methods in the GS algorithm to provide a solution. The results evidence the considerably better efficiency in iterating the SL model than applying the GS algorithm in finding a low energy value to the XY Hamiltonian.

2. Stuart-Landau versus Kuramoto networks

We additionally investigate the performance of the SL network at minimising the XY Hamiltonian in comparison to the fixed point solutions of the Kuramoto (KM) model. As mentioned in the manuscript, relating the steady states of the SL model with the minima of the XY Hamiltonian is a heuristic approach since, in general, oscillatory systems like lasers and driven-dissipative condensates have freely evolving amplitudes and therefore it demands investigation on how well such heuristic systems will perform in approximating the XY ground state energy. To backup this point, we show in 10(c) the average energy difference between the KM and the SL model in minimising the XY Hamiltonian over 1000 random dense graphs. Amazingly, around $N \approx 30$ spins (oscillators) the SL model starts outperforming the KM model. This means that the SL oscillators are much more efficient in exploring their state space during their transient growth phase from the initial "vacuum state" $|\psi_n(t = 0)| \simeq 0$ (in the context of quantum annealing) rather than the KM oscillators which are always locked onto the unit circle. Therefore, SL oscillators can clearly outperform KM oscillators at minimising the XY Hamiltonian of densely connected oscillator networks.

DATA AVAILABILITY

All data supporting this article is available on the University of Southampton's online repository (DOI: tbc).

[1] W. Lechner, P. Hauke, and P. Zoller, A quantum annealing architecture with all-to-all connectivity from local interactions, Science Advances **1**, e1500838 (2015), publisher: American Association for the Advancement of Science.

[2] S. Puri, C. K. Andersen, A. L. Grimsmo, and A. Blais, Quantum annealing with all-to-all connected nonlinear oscillators, Nat Commun **8**, 15785 (2017).

[3] V. Choi, Minor-embedding in adiabatic quantum computation: II. Minor-universal graph design, Quantum Inf Process **10**, 343 (2011).

[4] J. Cai, W. G. Macready, and A. Roy, A practical heuristic for finding graph minors, arXiv:1406.2741 [quant-ph] (2014), arXiv: 1406.2741.

[5] A. D. King and C. C. McGeoch, Algorithm engineering for a quantum annealing platform, arXiv:1410.2628 [quant-ph] (2014), arXiv: 1410.2628.

[6] D. Venturelli, S. Mandrà, S. Knysh, B. O'Gorman, R. Biswas, and V. Smelyanskiy, Quantum Optimization of Fully-Connected Spin Glasses, Phys. Rev. X **5**, 031040 (2015), arXiv: 1406.7553.

[7] A. Perdomo-Ortiz, A. Feldman, A. Ozaeta, S. V. Isakov, Z. Zhu, B. O'Gorman, H. G. Katzgraber, A. Diedrich, H. Neven, J. de Kleer, B. Lackey, and R. Biswas, Readiness of Quantum Optimization Machines for Industrial Applications, Phys. Rev. Applied **12**, 014004 (2019).

[8] R. Hamerly, T. Inagaki, P. L. McMahon, D. Venturelli, A. Marandi, E. Onodera, T.and Ng, C. Langrock, K. Inaba, T. Honjo, K. Enbutsu, T. Umeki, R. Kasahara, S. Utsunomiya, S. Kako, K. Kawarabayashi, R. L. Byer, M. M. Fejer, H. Mabuchi, D. Englund, E. Rieffel, H. Takesue, and Y. Yamamoto, Experimental investigation of performance differences between coherent Ising machines and a quantum annealer, Science Advances **5**, eaau0823 (2019), publisher: American Association for the Advancement of Science Section: Research Article.

[9] V. Choi, Minor-embedding in adiabatic quantum computation: I. The parameter setting problem, Quantum Inf Process **7**, 193 (2008).

[10] T. Boothby, A. D. King, and A. Roy, Fast clique minor generation in Chimera qubit connectivity graphs, Quantum Inf Process **15**, 495 (2016).

[11] N. G. Berloff, M. Silva, K. Kalinin, A. Askitopoulos, J. D. Töpfer, P. Cilibrizzi, W. Langbein, and o. G. Lagoudakis, Realizing the classical XY Hamiltonian in polariton simulators, Nature Mater **16**, 1120 (2017), number: 11 Publisher: Nature Publishing Group.

[12] O. Kyriienko, H. Sigurdsson, and T. C. H. Liew, Probabilistic solving of np-hard problems with bistable nonlinear optical networks, Phys. Rev. B **99**, 195301 (2019).

[13] S. Harrison, H. Sigurdsson, S. Alyatkin, J. Töpfer, and P. Lagoudakis, Solving the max-3-cut problem with coherent networks, Phys. Rev. Applied **17**, 024063 (2022).

[14] S. Luo, L. Liao, Z. Zhang, J. Wang, X. Shen, and Z. Chen, Classical Spin Chains Mimicked by Room-Temperature Polariton Condensates, Phys. Rev. Applied **13**, 044052 (2020).

[15] A. Kavokin, T. C. H. Liew, C. Schneider, P. G. Lagoudakis, S. Klembt, and S. Hoefling, Polariton condensates for classical and quantum computing, Nature Reviews Physics **4**, 435 (2022).

[16] R. Tao, K. Peng, L. Haeberlé, Q. Li, D. Jin, G. R. Fleming, S. Kéna-Cohen, X. Zhang, and W. Bao, Halide perovskites enable polaritonic xy spin hamiltonian at room temperature, Nature Materials 10.1038/s41563-022-01276-4 (2022).

[17] M. Vretenar, B. Kassenberg, S. Bissesar, C. Toebes, and J. Klaers, Controllable Josephson junction for photon Bose-Einstein condensates, Phys. Rev. Research **3**, 023167 (2021), publisher: American Physical Society.

[18] S. Tamate, Y. Yamamoto, A. Marandi, P. McMahon, and S. Utsunomiya, Simulating the classical xy model with a laser network (2016), arXiv:1608.00358 [physics.optics].

[19] Y. Takeda, S. Tamate, Y. Yamamoto, H. Takesue, T. Inagaki, and S. Utsunomiya, Boltzmann sampling for an XY model using a non-degenerate optical parametric oscillator network, Quantum Science and Technology **3**, 014004 (2017).

[20] S. Reifenstein, S. Kako, F. Khoyratee, T. Leleu, and Y. Yamamoto, Coherent Ising Machines with Optical Error Correction Circuits, Advanced Quantum Technologies **4**, 2100077 (2021).

[21] M. Honari-Latifpour, M. S. Mills, and M.-A. Miri, Combinatorial optimization with photonics-inspired clock models, Communications Physics **5**, 104 (2022).

[22] I. Gershenzon, G. Arwas, S. Gadasi, C. Tradonsky, A. Friesem, O. Raz, and N. Davidson, Exact mapping between a laser network loss rate and the classical xy hamiltonian by laser loss control, Nanophotonics **9**, 4117 (2020).

[23] A. N. K. Reddy, S. Mahler, A. Goldring, V. Pal, A. A. Friesem, and N. Davidson, Phase-locking of lasers with Gaussian coupling, arXiv:2106.02344 [physics] (2021), arXiv: 2106.02344.

[24] H. Goto, K. Tatsumura, and A. R. Dixon, Combinatorial optimization by simulating adiabatic bifurcations in nonlinear hamiltonian systems, Science Advances **5**, eaav2372 (2019).

[25] F. Böhm, T. V. Vaerenbergh, G. Verschaffelt, and G. Van der Sande, Order-of-magnitude differences in computational performance of analog Ising machines induced by the choice of nonlinearity, Communications Physics **4**, 149 (2021).

[26] A. Periwal, E. S. Cooper, P. Kunkel, J. F. Wienand, E. J. Davis, and M. Schleier-Smith, Programmable interactions and emergent geometry in an array of atom clouds, Nature **600**, 630 (2021).

[27] J. D. Töpfer, H. Sigurdsson, L. Pickup, and P. G. Lagoudakis, Time-delay polaritonics, Communications Physics **3**, 2 (2020).

[28] S. L. Harrison, H. Sigurdsson, and P. G. Lagoudakis, Synchronization in optically trapped polariton Stuart-Landau networks, Phys. Rev. B **101**, 155402 (2020).

[29] H. Sigurdsson, O. Kyriienko, K. Dini, and T. C. H. Liew, All-to-all intramodal condensate coupling by multifrequency excitation of polaritons, ACS Photonics **6**, 123 (2019).

[30] J. A. Acebrón, L. L. Bonilla, C. J. Pérez Vicente, F. Ritort, and R. Spigler, The Kuramoto model: A simple paradigm for synchronization phenomena, Rev. Mod. Phys. **77**, 137 (2005), publisher: American Physical Society.

[31] T. Leleu, Y. Yamamoto, S. Utsunomiya, and K. Aihara, Combinatorial optimization using dynamical phase transitions in driven-dissipative systems, Phys. Rev. E **95**, 022118 (2017).

[32] K. P. Kalinin and N. G. Berloff, Networks of non-equilibrium condensates for global optimization, New Journal of Physics **20**, 113023 (2018).

[33] Y. Kuramoto, Self-entrainment of a population of coupled non-linear oscillators, in *International Symposium on Mathematical Problems in Theoretical Physics*, Lecture Notes in Physics, edited by H. Araki (Springer, Berlin, Heidelberg, 1975) pp. 420–422.

[34] S. H. Strogatz, From Kuramoto to Crawford: exploring the onset of synchronization in populations of coupled oscillators, Physica D: Nonlinear Phenomena **143**, 1 (2000).

[35] N. Mohseni, P. L. McMahon, and T. Byrnes, Ising machines as hardware solvers of combinatorial optimization problems, Nature Reviews Physics **4**, 363 (2022).

[36] The resulting triad graph consists of vertex set: $V^{\mathrm{emb}}(K_N^{\mathrm{emb}})$ containing $N(N-1)$ vertices V_n^{emb}, and edge set: $J^{emb}(K_N^{\mathrm{emb}})$ containing $\frac{N(N-1)}{2}$ inter-chain edges $J_{n,m}^{\mathrm{inter}}$ and $N(N-2)$ intra-chain edges $J_{n,m}^{\mathrm{intra}}$.

[37] K. L. Pudenz, Parameter setting for quantum annealers, in *2016 IEEE High Performance Extreme Computing Conference (HPEC)* (2016) pp. 1–6.

[38] E. Pelofske, G. Hahn, and H. Djidjev, Advanced unembedding techniques for quantum annealers, arXiv:2009.05028 [quant-ph] (2020), arXiv: 2009.05028.

[39] S. H. Strogatz and R. E. Mirollo, Stability of incoherence in a population of coupled oscillators, J Stat Phys **63**, 613 (1991).

[40] Y. Kuramoto, Chemical Oscillations, Waves, and Turbulence (Springer, Berlin, Heidelberg, 1984) pp. 68–77.

[41] D. J. Wales and J. P. K. Doye, Global optimization by basin-hopping and the lowest energy structures of lennard-jones clusters containing up to 110 atoms, The Journal of Physical Chemistry A **101**, 5111 (1997).

[42] A. Townsend, M. Stillman, and S. H. Strogatz, Dense networks that do not synchronize and sparse ones that do, Chaos: An Interdisciplinary Journal of Nonlinear Science **30**, 083142 (2020).

[43] Y. Inui, M. D. S. H. Gunathilaka, S. Kako, T. Aonishi, and Y. Yamamoto, Control of amplitude homogeneity in coherent ising machines with artificial zeeman terms, Communications Physics **5**, 154 (2022).

[44] https://uk.mathworks.com/help/gads/how-globalsearch-and-multistart-work.html.

[45] https://uk.mathworks.com/help/gads/.